PHYSICAL REVIEW APPLIED **15,** 064019 (2021)

Alternation of Magnetic Anisotropy Accompanied by Metal-Insulator Transition in Strained Ultrathin Manganite Heterostructures

Masaki Kobayashi,[1,2,*] Le Duc Anh,[1,3,4] Masahiro Suzuki,[5] Shingo Kaneta-Takada,[1]
Yukiharu Takeda,[6] Shin-ichi Fujimori,[6] Goro Shibata,[7] Arata Tanaka,[8] Masaaki Tanaka,[1,2]
Shinobu Ohya,[2,3] and Atsushi Fujimori[5,6,9]

[1] *Department of Electrical Engineering and Information Systems, The University of Tokyo, 7-3-1 Hongo, Bunkyo-ku, Tokyo 113-8656, Japan*
[2] *Center for Spintronics Research Network, The University of Tokyo, 7-3-1 Hongo, Bunkyo-ku, Tokyo 113-8656, Japan*
[3] *Institute of Engineering Innovation, Graduate School of Engineering, The University of Tokyo, 7-3-1 Hongo, Bunkyo-ku, Tokyo 113-8656, Japan*
[4] *PRESTO, JST, 4-1-8 Honcho, Kawaguchi, Saitama, 332-0012, Japan*
[5] *Department of Physics, The University of Tokyo, 7-3-1 Hongo, Bunkyo-ku, Tokyo 113-0033, Japan*
[6] *Materials Sciences Research Center, Japan Atomic Energy Agency, Sayo-gun, Hyogo 679-5148, Japan*
[7] *Department of Applied Physics, Tokyo University of Science, Katsushika, Tokyo 125-8585, Japan*
[8] *Quantum Matter Program, Graduate School of Advanced Science and Engineering, Hiroshima University, Higashi-Hiroshima 739-8530, Japan*
[9] *Department of Applied Physics, Waseda University, Okubo, Shinjuku, Tokyo 169-8555, Japan*

(Received 24 September 2020; revised 31 March 2021; accepted 5 May 2021; published 8 June 2021)

A fundamental understanding of the interfacial magnetic properties in ferromagnetic heterostructures is essential for utilizing ferromagnetic materials for spintronic device applications. Here, we investigate the interfacial magnetic and electronic structures of epitaxial single-crystalline $LaAlO_3$(LAO)/$La_{0.6}Sr_{0.4}MnO_3$(LSMO)/Nb:$SrTiO_3$(Nb:STO) heterostructures with varying LSMO layer thicknesses, in which the magnetic anisotropy strongly changes with the LSMO thickness due to the delicate balance between strains originating from both the Nb:STO and LAO layers, using x-ray magnetic circular dichroism and photoemission spectroscopy. We successfully detect the clear change of the magnetic behavior of the Mn ions concomitant with the thickness-dependent metal-insulator transition. Our results suggest that the double-exchange interaction induces ferromagnetism in the metallic LSMO film under tensile strain caused by the STO substrate, while the superexchange interaction determines the magnetic behavior in the insulating LSMO film under compressive strain originating from the top LAO layer. The change in strain, depending on LSMO layer thickness, is confirmed by scanning transmission electron microscopy. Based on those findings, the formation of a magnetic dead layer near the LAO/LSMO interface is attributed to competition between the superexchange interaction via Mn $3d_{3z^2-r^2}$ orbitals under compressive strain and the double-exchange interaction via the $3d_{x^2-y^2}$ orbitals. These findings provide key aspects of ferromagnetic oxide heterostructures for the development of spintronic device applications.

DOI: 10.1103/PhysRevApplied.15.064019

I. INTRODUCTION

Oxide electronics attracts considerable interest because of a variety of potential applications in both electronics and spintronics and because we are provided with the opportunity to understand the rich fundamental physics of strongly correlated electron systems [1]. In heterostructures with transition-metal perovskite oxides, the complex interplay among multiple degrees of freedom of the correlated electrons yields unusual quantum phenomena, such as superconductivity, colossal magnetoresistance, and high-mobility two-dimensional electron-hole gas [2–5]. Recently, an intriguing spintronics functionality was demonstrated in ferromagnetic perovskite oxide (La,Sr)MnO_3 (LSMO)-based devices; it was clarified that the magnetic anisotropy of LSMO could be manipulated with extremely low power consumption [6–10]. For such heterostructures, spin and charge modulations at the interfaces are considered to modify the physical

---

[*] masaki.kobayashi@ee.t.u-tokyo.ac.jp

properties of the interfaces from that of bulk materials [11]. Knowledge of the interfacial magnetic and electronic properties of ferromagnetic oxide heterostructures is indispensable for improving the performance of spintronics devices.

The ferromagnetic oxide LSMO is one of the promising materials for spintronics because of its distinctive physical properties, such as colossal magnetoresistance, half-metallicity nature, and high Curie temperatures above room temperature [12,13]. Peculiar physical properties of LSMO, including the metal-insulator transition (MIT), originate from a complex interplay among the charge, spin, and orbital degrees of freedom [14,15]. In single-crystalline LSMO thin films and heterostructures, the electronic and magnetic properties of the LSMO layers are strongly affected by a reduction of dimensionality, epitaxial strain from the substrate or adjacent layers, and disorder at the surface or interface [11,16,17]. These external effects lead to the formation of a “magnetic dead layer” near the surface or interface, where ferromagnetism is suppressed [16,18]. Previous studies on LSMO thin films under epitaxial strains or with varying thicknesses have reported that spatial magnetic inhomogeneity, leading to phase separation, is intimately related to the formation of the magnetic dead layers in LSMO heterostructures [19–21]. To understand the origin of the magnetic dead layer and the relationship between epitaxial strain and the formation of the magnetic dead layer, it is important to investigate high-quality crystalline LSMO layers with atomically abrupt interfaces. In particular, the magnetic behavior of ultrathin LSMO layers under epitaxial strain is key for the application of ferromagnetic oxide heterostructures for spintronics devices on the nanometer scale.

Here, we investigate the magnetic and electronic states at the interface between LSMO and $LaAlO_3$ (LAO) layers that are epitaxially grown on Nb-doped $SrTiO_3$ (Nb:STO) substrates, namely, LAO/LSMO/Nb:STO heterostructures with varying thicknesses of the LSMO layer using x-ray magnetic circular dichroism (XMCD) and photoemission spectroscopy (PES). Here, the magnetic anisotropy of the LSMO layer depends on its thickness due to the delicate balance between strains originating from both the STO and LAO layers. The atomically abrupt interfaces enable us to observe the intrinsic interfacial electronic structure. Our experimental findings demonstrate changes in the magnetic behavior accompanying the MIT in the strained ultrathin LSMO layers, providing a mechanism for the formation of the magnetic dead layer at interfaces in ferromagnetic oxide heterostructures.

II. EXPERIMENT

Digitally controlled LAO(2 u.c.)/LSMO(t u.c.) ($t = 5$, 10, and 15; u.c. denotes a unit cell) heterostructures are epitaxially grown on atomically flat (001) surfaces of

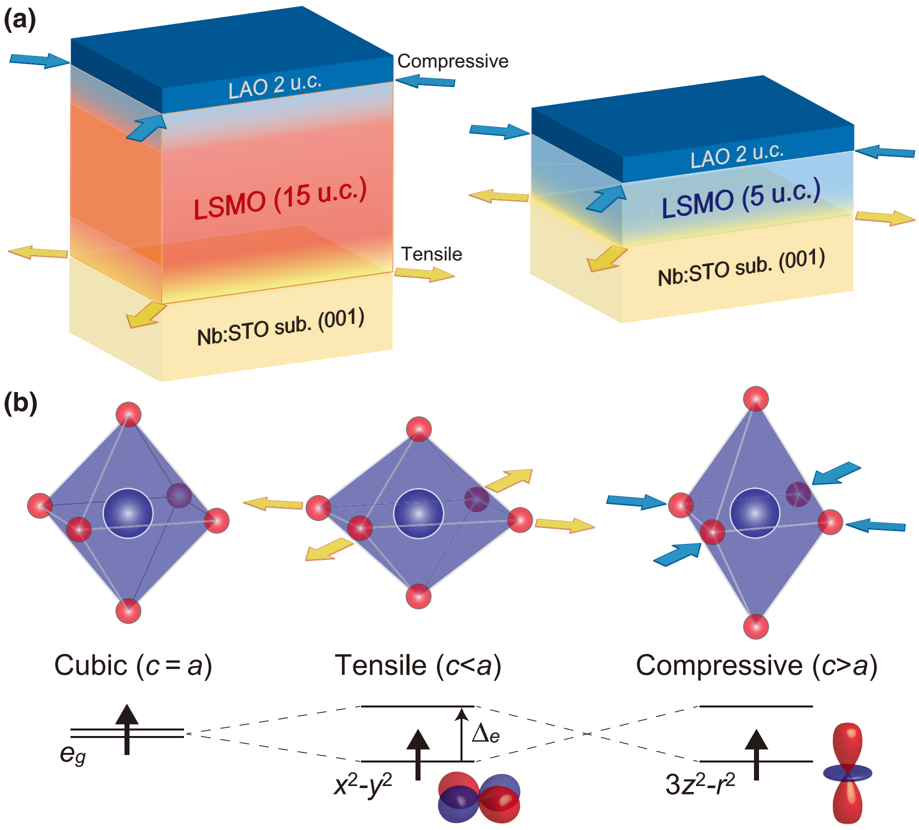

FIG. 1. Schematic pictures of LAO/LSMO/Nb:STO heterostructures. (a) Sample structures of LAO/LSMO/Nb:STO heterostructures with thicknesses of 15 (left) and 5 u.c. (right). Arrows denote directions of strains. (b) $Mn^{3+}O_6$ cluster with and without strains. Energy diagram of 3d e_g states under tensile and compressive strains also shown. Δ_e denotes crystal-field splitting of the e_g states under strains.

TiO_2-terminated Nb:STO substrates by molecular-beam epitaxy (MBE). The LAO top layer protects the surface from further oxidization. Details of the growth conditions are described elsewhere [9]. Sample structures of the LAO/LSMO/Nb:STO heterostructures are shown in Fig. 1(a). The magnetic properties of the heterostructures are measured using a superconducting quantum interference device (SQUID) magnetometer. Scanning tunneling electron microscopy (STEM) and electron energy-loss spectroscopy (EELS) experiments are performed using a JEM-ARM200F (JEOL Ltd.) microscope operated at 200 kV (MST Ltd.). The depth resolution of EELS is about 1 nm. The PES and XMCD experiments are performed at the helical undulator beamline BL23SU of SPring-8 [22–24]. The monochromator resolution, $E/\Delta E$, is 10 000. For XMCD measurements, absorption spectra for circularly polarized x-rays with the photon helicity parallel (μ^+) and antiparallel (μ^-) to the spin polarization are taken by reversing the photon helicity at each photon energy, $h\nu$, and are recorded in total-electron-yield mode. The μ^+ and μ^- spectra are taken for both positive and negative applied magnetic fields and are averaged to eliminate experimental errors, such as spurious dichroic signals arising from the slightly different optical paths for the two circular polarizations. External magnetic fields are applied perpendicular to the sample surfaces (the [001] direction). To estimate the integrated values of the X-ray absorption spectroscopy (XAS) spectra at the Mn $L_{2,3}$ edge, hyperbolic tangent functions are subtracted from the spectra as backgrounds. For the PES measurements, the samples are kept at 20 K under an ultrahigh vacuum better than 10^{-8} Pa. The total energy resolution, including temperature broadening, is about 150 meV. The position of the Fermi level (E_F) is determined by measuring evaporated gold that is electrically in contact with the samples. To discuss the origin of magnetic anisotropy, cluster-model calculations are conducted based on a method described elsewhere [25], assuming tensile ($c < a$) or compressive ($c > a$) strain (D_{4h} crystal fields).

III. RESULTS AND DISCUSSION

Figure 2 shows the magnetic field dependence of the magnetization (M) of the heterostructures measured by the SQUID magnetometer. The out-of-plane linear magnetic susceptibility, including the diamagnetic contribution from the substrates, for $t = 5$ u.c. is positive, while that for $t = 15$ u.c. is negative [see the red curves in Figs. 2(a) and 2(b)]. This indicates that there are a considerable amount of paramagnetic Mn ions for $t = 5$ u.c.. Figures 2(c) and 2(d) show the magnetization curves obtained for $t = 5$ and 15 u.c., respectively, after subtracting the abovementioned linear components. To remove the

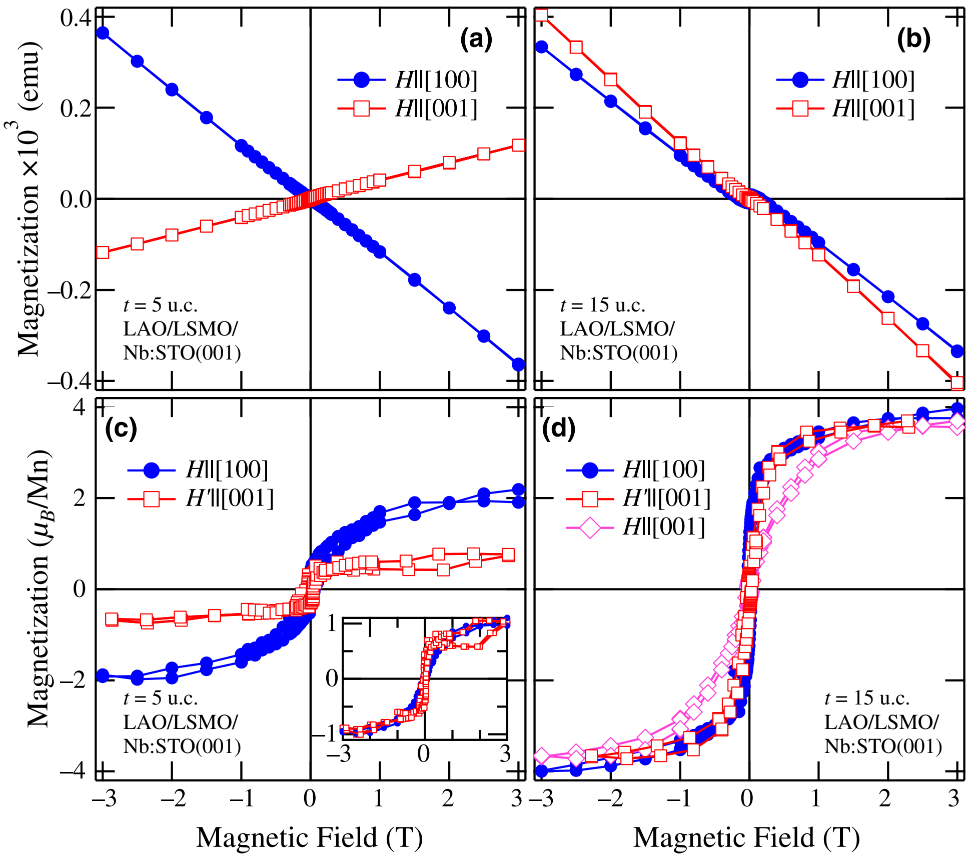

FIG. 2. M-H curves of LAO/LSMO/Nb:STO heterostructures measured by SQUID. The measurements have been performed at 10 K. (a),(b) Raw M-H curves of 5 and 15 u.c. samples, respectively. Magnetic fields are applied to parallel to the in-plane [100] and out-of-plane [001] directions. (c),(d) H dependence of ferromagnetic components of 5 and 15 u.c. samples, respectively. Here, linear components are subtracted from M-H curves. Inset of (c) shows normalized magnetization curves. Open squares and rhombi denote out-of-plane M-H curves with (H') and without demagnetization-field correction, respectively.

effects of the magnetic shape anisotropy, the demagnetization fields are corrected for the out-of-plane magnetization curves by using the equation $H' = H - M$ (A/m), where H is the applied external magnetic field strength and H' is the magnetic field strength corrected for the demagnetization field [see Fig. 2(d)]. It should be noted here that the saturation magnetization for $t = 15$ u.c. is about 4 μ_B/Mn, nearly the full magnetic moment per Mn atom, suggesting that nearly all Mn ions contribute to ferromagnetism. In contrast, the saturation magnetization is much smaller than the full moment for $t = 5$ u.c., as shown in Fig. 2(c). For $t = 5$ u.c., the out-of-plane susceptibility near the zero field is much larger than the in-plane one, as shown in the inset of Fig. 2(c), indicating perpendicular magnetic anisotropy. The most important point here is that the easy magnetization axis is changed with t, i.e., the film with $t = 5$ u.c. has perpendicular magnetic anisotropy, while the one with $t = 15$ u.c. has in-plane magnetic anisotropy.

To understand the thickness-dependent magnetic anisotropy of the LAO/LSMO/Nb:STO heterostructures, we obtain a crystal-lattice image with atomic resolution using STEM EELS. Figures 3(a) and 3(b) show high-angle annular dark-field (HAADF) STEM images of the heterostructures for $t = 5$ and 15 u.c., respectively, indicating that the heterostructures are composed of coherently grown single-crystal layers with abrupt heterointerfaces. The ratio of the out-of-plane (c axis) to in-plane (a axis) lattice constants (c/a) estimated from the atomic resolution image is $c/a = 0.985$ for the 15-u.c. film, indicating that the LSMO layer in the heterostructure is under tensile strain. From this point of view, the heterostructure for $t = 15$ u.c. is similar to that of bulk LSMO films grown on STO. In contrast, the ratio of c/a for the 5-u.c. film is 1.034, indicating that the LSMO layer is under compressive strain. In the LAO/LSMO/Nb:STO heterostructure, compressive strain is predominant because the lattice mismatch of LSMO with LAO of about 3% is considerably larger than that with STO of about 1% [26]. Figures 3(c) and 3(d) show the depth profiles of the concentration of each atom for the heterostructures obtained using EELS. The results indicate that the chemical composition of each layer in the heterostructure is approximately uniform and there is a compositional mixture within a few u.c. of the heterointerfaces.

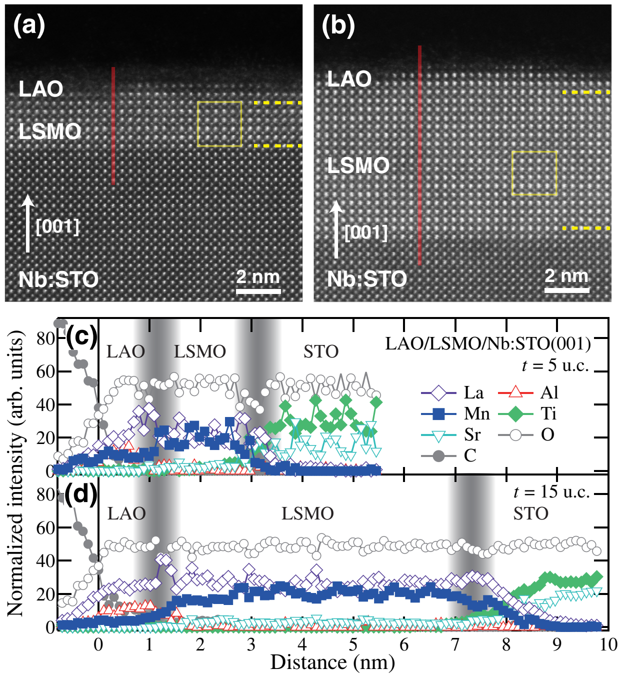

FIG. 3. STEM EELS analysis for the LAO/LSMO/Nb:STO heterostructures. (a),(b) HAADF STEM lattice images of 5 and 15 u.c. samples, respectively. Dashed horizontal lines denote interfaces between layers. Rectangles are guides for the change of lattice constants (c/a). (c),(d) Depth profiles of normalized EELS intensity in heterostructures for $t = 5$ and 15 u.c., respectively. Profiles are obtained along solid lines in (a),(b). Here, depth resolution of STEM EELS is about 1 nm. Shaded areas denote intermixing regions near interfaces.

To elucidate the origin of the magnetic anisotropy of the LAO/LSMO/Nb:STO heterostructures, the single-ion magnetic anisotropy energy (ΔE_{MA}) of the Mn^{3+} ion is estimated using the ratio of the lattice constants, c/a, under strains. Considering that the splitting, Δ_e, of the e_g states [see Fig. 1(b)] is proportional to the square of p–d transfer integrals divided by the charge-transfer energy and that the Slater-Koster parameter ($pd\sigma$) is proportional to the power of the Mn-O atomic distance r, $r^{-7/2}$ [27], the value of Δ_e is estimated to be +55 meV for the tensile strain of the $t = 15$ u.c. sample and −121 meV for the compressive strain of the $t = 5$ u.c. sample. Here, the positive (negative) sign of Δ_e means that the x^2-y^2 ($3z^2$-r^2) orbital is preferentially occupied. Cluster-model calculations [25] are performed for the Mn^{3+}O$_6$ cluster in LSMO to estimate ΔE_{MA} using the Δ_e values given above. Here, the electronic structure parameters (charge-transfer energy, d–d Coulomb interaction, Slater-Koster parameter, etc.) for the calculations are the same as those reported in Ref. [28]. The values of ΔE_{MA} estimated are listed in Table I, where the positive (negative) value means the perpendicular (in-plane) easy magnetization axis. The values of ΔE_{MA} are calculated as the differences of the total energies obtained with magnetization along the in-plane [100] and out-of-plane [001] directions. This indicates that the preferential occupation of the $d_{3z^2-r^2}$ orbital under compressive strain favors spin orientation perpendicular to the a-b plane, while that of the $d_{x^2-y^2}$ orbital under tensile strain favors spin orientation with an in-plane easy axis. Thus, the calculated magnetocrystalline anisotropy is qualitatively consistent with the change of the easy magnetization axis, depending on strains. The experimental magnetic anisotropy energies are estimated from the difference

TABLE I. Single-ion magnetic anisotropy energies of the LAO/LSMO/Nb:STO heterostructures. c/a are estimated from the HAADF STEM images [Figs. 3(a) and 3(b)]. Considering splitting of the e_g states (Δ_e) obtained from strains (the in-plane and out-of-plane lattice constants), the values of the magnetic anisotropy energy (ΔE_{MA}) of these heterostructures are estimated using cluster-model calculations [25]. Here, Δ_e is defined as the energy difference between $3z^2$-r^2 and x^2-y^2 orbitals: $\Delta_e = E_{3z^2-r^2} - E_{x^2-y^2}$. The positive (negative) sign of Δ_e means that the x^2-y^2 ($3z^2$-r^2) orbital is preferentially occupied [Fig. 1(b)].

Sample	c/a	Δ_e (meV)	ΔE_{MA} (calc.) (meV)
$t = 5$ u.c.	1.034	−121	4.56
$t = 15$ u.c.	0.985	55	−2.01

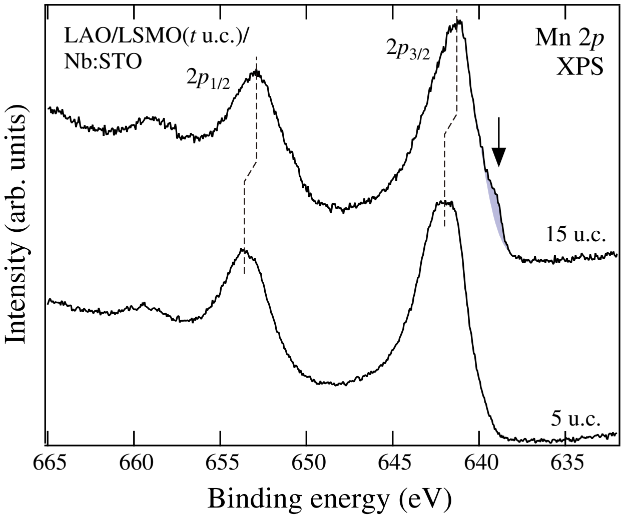

FIG. 4. Mn $2p$ XPS spectra of LAO/LSMO/Nb:STO heterostructures. Here, incident photon energy is $h\nu = 1200$ eV. Spectra are normalized to maximum height and a vertical offset put on the spectrum of the film for 15 u.c. Shaded area denoted by an arrow is a well-screened peak. Vertical dashed lines are guides to the eye.

between the integrals of the normalized M-H curves with H applied in the film plane ([100]) and perpendicular to the film plane ([001]) directions: $\int \mu_0(H_{\mathrm{out}} - H_{\mathrm{in}})dM$, where μ_0 is the vacuum permeability. The estimated values of ΔE_{MA} are +0.077 and −0.040 meV for $t = 5$ and 15 u.c., respectively. By comparing the experimental and theoretical values of ΔE_{MA}, although the magnitudes of ΔE_{MA} are apparently overestimated in the calculations, the directions of the easy magnetization axes can be qualitatively explained.

Since the magnetic property of LSMO is related to not only the single-ion magnetocrystalline anisotropy, but also intersite magnetic interactions, such as the double-exchange interaction, knowledge of the electronic structure and transport property is indispensable to understand the details of the magnetic behavior of LAO/LSMO/Nb:STO heterostructures. To reveal changes in the electronic structure with changing the LSMO thickness, we perform x-ray photoemission spectroscopy (XPS) for core levels and resonant photoemission spectroscopy (RPES) for the valence band (VB). Figure 4 shows the Mn $2p$ core-level XPS spectra of the LAO/LSMO heterostructures. Notably, a small peak (well-screened peak) appears on the low binding-energy (E_B) side of the $2p_{3/2}$ peak only for $t = 15$ u.c. This well-screened feature of the Mn $2p$ spectrum originates from screening of the $2p$ core hole by ferromagnetic metallic electrons in the LSMO layer [29]. The appearance of this peak reflects the increase of the metallicity of the 15 u.c. LSMO layer. In previous PES studies of LSMO thin films [29,30], the well-screened peaks observed in hard x-ray PES with high bulk sensitivity were larger than those in soft x-ray PES, probably because of defects or disorder near the surface or interface. Thus, the observation of the well-screened peak with soft x-ray PES in the present study is consistent with the high-quality crystallinity of the LAO/LSMO/Nb:STO heterostructures with atomically abrupt interfaces confirmed by STEM. In addition, if one compares the main peaks of the Mn $2p$ spectra, a core-level shift, depending on the thickness of the LSMO layer, is identified (see dashed lines in Fig. 4).

Figures 5(a) and 5(b) show the off-resonance photoemission spectra of the VB taken at $h\nu = 637$ eV for the LAO/LSMO/Nb:STO heterostructures. It should be noted here that there is a gap at E_F for $t = 5$ u.c., while the spectrum for $t = 15$ u.c. has a finite density of states at E_F, that is, the MIT occurs at a thickness between $t = 5$ and 15 u.c. This is analogous to the thickness-dependent MIT in LSMO layers sandwiched between STO [17]. The observations indicate that the core-level shift observed in the Mn $2p$ spectra reflects the chemical-potential shift accompanied by the MIT because the shift of the Mn $2p$ spectra is comparable to that of the VB spectra. Since the EELS observations imply that there are La-rich regions near the LAO/LSMO interfaces [see Figs. 3(c) and 3(d)], changes in the chemical compositions near the interfaces may also contribute to the chemical-potential shift. To reveal the changes of the Mn $3d$ states across the MIT in detail, the Mn $2p$-$3d$ RPES spectra taken at $h\nu = 642.5$ eV are shown in Figs. 5(c) and 5(d). In contrast to the insulating state for $t = 5$ u.c., the metallic nature of the Mn $3d$ states for $t = 15$ u.c. is obvious: the finite density of states at E_F and the asymmetric shape of the peak at $E_B \sim 2$ eV, which indicates the effects of screening and in line with the appearance of the well-screened peak in the Mn $2p$ spectrum of the 15-u.c. film, as shown in Fig. 4. This is consistent with the appearance of the well-screened feature observed in the Mn $2p$ spectrum for $t = 15$ u.c. shown in Fig. 4. Thus, we consider that the thickness-dependent

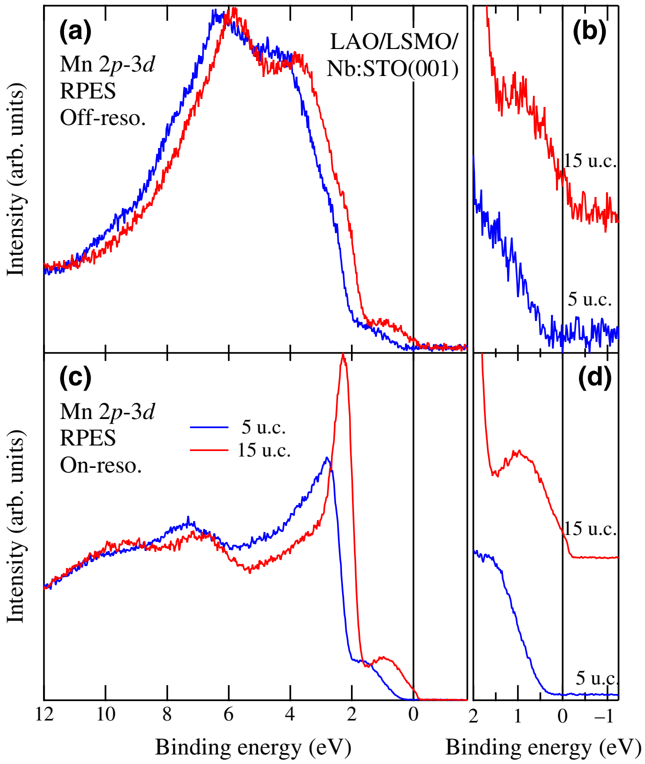

FIG. 5. Mn $2p$-$3d$ RPES of LAO/LSMO/Nb:STO heterostructures. (a) Off-resonance spectra taken at $h\nu = 637$ eV (at the black arrow shown in Fig. 6(a)). Spectra are normalized to the maximum height. (b) Enlarged plot near E_F of the off-resonance spectra. (c) On-resonance spectra taken at $h\nu = 642.5$ eV (at the red arrow shown in Fig. 6(a)). (d) Enlarged plot near E_F of the on-resonance spectra. The on-resonance spectra are normalized to background heights around $E_B \sim 12$ eV.

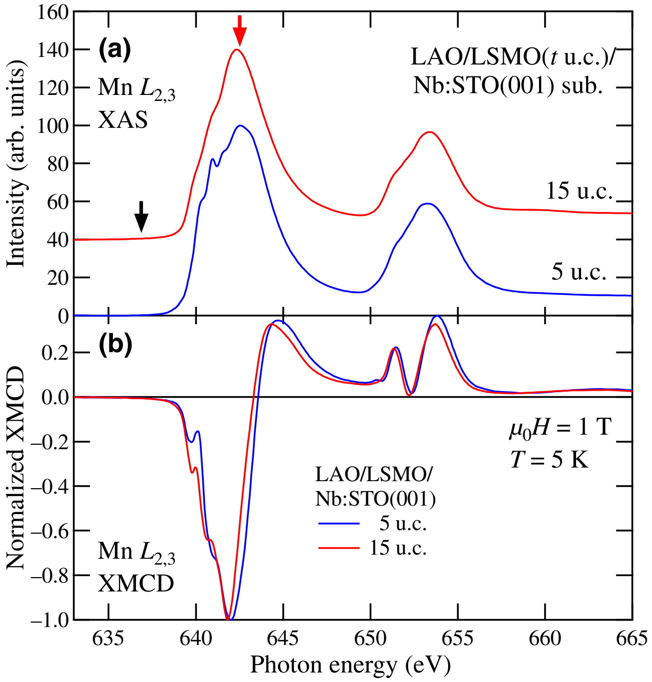

FIG. 6. Mn $L_{2,3}$-edge absorption spectra of LAO/LSMO/Nb:STO heterostructures. (a) XAS spectra. Intensities are normalized to maximum height of 100. Red and black arrows denote excitation energies for off-resonance (637 eV) and on-resonance (642.5 eV) spectra, respectively. (b) XMCD spectra. Spectra are measured at $\mu_0H = 1$ T and $T = 5$ K. To compare spectral line shapes, spectra are normalized to minimum intensity.

MIT observed in the heterostructure predominantly originates from the intrinsic nature of the Mn $3d$ state in the LSMO layer.

Figure 6 shows Mn $L_{2,3}$ XAS and XMCD spectra of the LAO/LSMO/Nb:STO heterostructures measured at a magnetic field, μ_0H, of 1 T applied perpendicular to the films and at a temperature of $T = 5$ K. In general, the line shapes of the XAS and XMCD spectra reflect the local electronic and magnetic properties. The XAS and XMCD spectra of the 15-u.c. sample are similar to those of thick LSMO layers on STO substrates [31]. This result indicates that the LSMO layer with $t = 15$ u.c. in our LAO/LSMO/Nb:STO heterostructure has nearly the same electronic structure as that of thick LSMO layers under tensile strain reported previously [26,28,31,32]. In contrast, the XAS spectrum of the 5-u.c. film is different from that of the 15-u.c. film, but is similar to that of thick LSMO layers deposited on LAO substrates [26,28,32], suggesting that the 5-u.c. LSMO layer is compressively strained by the top LAO layer. These spectral changes are consistent with structural changes of c/a confirmed by STEM, as shown in Fig. 3. The strongest XAS peak for $t = 15$ u.c. is located at slightly lower energy than that for $t = 5$ u.c., which is similar to the shift of the main peaks observed for LSMO/LAO and LSMO/STO [33]. Notably, this peak shift is opposite to the thickness dependence of LSMO/STO [31]. Comparing the line shapes of the XMCD spectra for different LSMO thicknesses, as shown in Fig. 1(b), the electronic structure of the LSMO layer clearly changes as the thickness decreases from 15 to 5 u.c.

Figures 7(a) and 7(b) show the H dependence of the XMCD spectra of the LAO/LSMO($t = 15$ and 5 u.c.)/Nb:STO heterostructures, respectively. The XMCD intensities increase with increasing H. As for the XMCD line shapes, they are approximately independent of H for the 15-u.c. film [inset of Fig. 7(a)], while there are appreciable spectral line-shape changes with H around 640 eV for the 5-u.c. film [inset of Fig. 7(b)]. This means that a paramagnetic component exists in the 5-u.c. film in addition to the ferromagnetic component, while almost all Mn ions contribute to ferromagnetism in the 15-u.c. film. Notably, the XMCD intensity for $t = 15$ u.c. is much larger than that for $t = 5$ u.c., which is consistent with magnetization measured by SQUID, as shown in Fig. 2. Figures 7(c) and 7(d) show the H and T dependences of

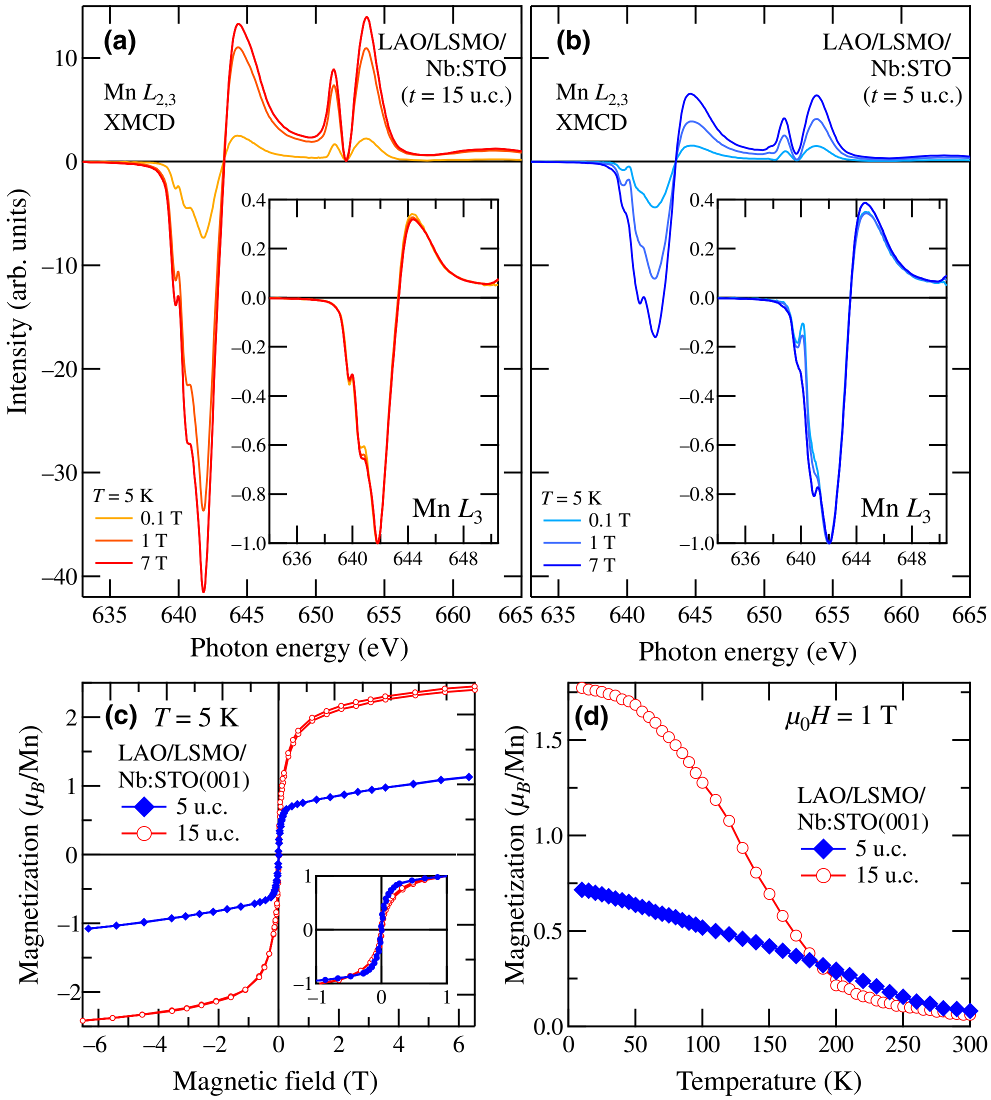

FIG. 7. Magnetic field and temperature dependences of Mn $L_{2,3}$ XMCD spectra of LAO/LSMO/Nb:STO heterostructures. Here, magnetic field is applied perpendicular to films. (a),(b) H dependence of XMCD spectra measured at $T = 5$ K for LSMO films with thicknesses of 15 and 5 u.c., respectively. Scale of vertical axes is the same as that in Fig. 6(a), where XAS intensities are normalized to maximum height of 100. Insets show XMCD spectra normalized to minimum intensity. (c) H dependence of magnetization at $T = 5$ K estimated using XMCD sum rules. Inset shows same data normalized at $\mu_0H = 1$ T. (d) T dependence of magnetization at $\mu_0H = 1$ T. For magnetizations shown in (c),(d), demagnetization fields are corrected.

the XMCD intensities of the LAO/LSMO/Nb:STO heterostructures, respectively. As one can see, the magnetic behavior is clearly different between the thin and thick LSMO films. The magnetization curve for $t = 5$ u.c. is rapidly saturated, in comparison with that for $t = 15$ u.c., although the saturation magnetization per Mn ion of the film for $t = 5$ u.c. is as small as one third of that for $t = 15$ u.c., as shown in Fig. 7(c). While the magnetization for $t = 15$ u.c. rapidly decreases with increasing T, that for $t = 5$ u.c. only gradually decreases with increasing T, as shown in Fig. 7(d). Considering the observations using SQUID shown in Fig. 2, this result likely reflects the change of the magnetic anisotropy with changing t. In thick LSMO films grown on STO substrates, the double-exchange interaction between Mn^{3+} and Mn^{4+} ions stabilizes ferromagnetism with an in-plane easy magnetization axis due to the preferential occupation of the x^2-y^2 orbital under tensile strain [27,34]. In our work, these bulklike magnetic properties are consistently observed in the thick 15-u.c. film. In contrast, the magnetic behaviors of the film for $t = 5$ u.c. are completely different from those reported for single LSMO films grown on STO [34].

The XMCD and RPES results for the LAO/LSMO/Nb:STO heterostructures with varying the LSMO layer thickness indicate changes to the magnetic behavior accompanied by the MIT. For bulk LSMO and thick LSMO films, ferromagnetism arises from the double-exchange interaction [35] between Mn^{3+} and Mn^{4+} ions, which leads to the colossal magnetoresistance concomitant with the MIT [15]. As shown in Fig. 1(b), under tensile strain from the STO substrate, the x^2-y^2 orbital of the e_g states is preferentially occupied by conduction electrons, leading to magnetic anisotropy with the in-plane [110] (or [100]) easy magnetization axis. In contrast to the nearly full moment in the 15-u.c. LSMO layer observed by SQUID and XMCD, the saturation magnetization of the 5-u.c. LSMO film is much smaller than that of the full moment [see Figs. 2(c), 2(d), 7(c), and 7(d)]. This may arise from the superexchange interaction, which plays an essential role in the magnetism of the insulating phase of the ultrathin LSMO layer, where the *d* electrons are localized. Under compressive strain from the LAO layer, the $d_{3z^2-r^2}$ orbital of the Mn^{3+} ion is preferentially occupied, as shown in Fig. 1(b), resulting in magnetic anisotropy with the out-of-plane [001] easy magnetization axis. The superexchange interaction path, Mn^{4+}-O-Mn^{3+}, in the out-of-plane direction, involving the $d_{3z^2-r^2}$ orbital, is expected to be ferromagnetic, while the same interaction within the plane is antiferromagnetic [36]. It follows from these arguments that the change in magnetic anisotropy and reduction of magnetization accompanying the MIT originate from compressive strain in the LSMO layer.

Whereas most of the Mn ions contribute to ferromagnetism in the metallic LSMO layer, only a part of the Mn ions contribute to the ferromagnetism in the insulating LSMO layer. From the M-H curve of the heterostructure with $t = 5$ u.c. shown in Fig. 7(c), the saturation magnetization and the paramagnetic susceptibility, χ, in high magnetic fields ($\mu_0 H > 1$ T) are estimated to be about 0.72 μ_B/Mn and 5.23×10^2 μ_B/Mn/T, respectively. The saturation magnetization is nearly identical to that estimated from the macroscopic SQUID measurements shown in Fig. 2(c); this indicates that only 25% of the total Mn ions contribute to ferromagnetism. The rest of Mn ions may be coupled with each other antiferromagnetically through the superexchange interaction via the Mn^{4+}-O-Mn^{4+} or Mn^{3+}-O-Mn^{3+} paths. Under compressive strain, the preferential occupation of the $d_{3z^2-r^2}$ orbital in the LSMO layer favors spin orientation perpendicular to the *a*-*b* plane (see also Table I) [16,26,37]. This is evident in the SQUID results shown in Figs. 2(a) and 2(b), where the out-of-plane [001] paramagnetic susceptibility, including the diamagnetic contribution from the substrate, is positive in the insulating heterostructure for $t = 5$ u.c., but negative in the ferromagnetic heterostructure for $t = 15$ u.c.. We note that the in-plane [100] paramagnetic susceptibility is negative in both cases ($t = 5$ and 15 u.c.). By analyzing the paramagnetic susceptibility, χ, using the Curie-Weiss law, $\chi(T) = C/(T - \theta)$, where C is the Curie constant and θ is the Weiss temperature, under the assumption that 75% of the Mn ions are paramagnetic, the Weiss temperature is estimated to be approximately -150 K. The negative Weiss temperature is qualitatively consistent with antiferromagnetic superexchange via the Mn^{3+}-O-Mn^{3+} path. Therefore, occupation of the $d_{3z^2-r^2}$ orbital under compressive strain [see Fig. 1(b)] can explain why the paramagnetic susceptibility appears preferentially for the out-of-plane direction in the insulating heterostructure.

The present experimental findings may provide key knowledge to understand the formation of a magnetic dead layer near the LAO/LSMO interface. In the metallic LSMO case, when the interface is not ideal and has extrinsic defects, such as atomic intermixing and structural deformation [11,32], the conduction electrons are scattered by these defects and disorder, resulting in weakening of the double-exchange interaction [38]. In addition to compressive strain, oxygen octahedral rotation (OOR) for the LSMO layers is induced by the top LAO layer [9,39,40]. The OOR slightly reduces the in-plane bond angle of the Mn-O-Mn path in the vicinity of the interface, which also weakens the double-exchange interaction. As a consequence, competition between the double-exchange and superexchange interactions, depending on strain, leads to the formation of the magnetic dead layer near the interface.

For the origin of the magnetic dead layer at the interfaces of LSMO thin films under tensile strain, phase-separation models are proposed [19–21]. In a previous XMCD study on the thickness-dependent MIT in a LSMO/STO heterostructure [31], it has been revealed that paramagnetic, superparamagnetic, and ferromagnetic phases coexist in the magnetic dead layer. Magnetic inhomogeneity or phase separation is probably associated with spatial fluctuation of the hole distribution and superexchange interaction in the LSMO layer. In the present case of the insulating LSMO film under compressive strain, it is likely that the ferromagnetic and superparamagnetic phases arise from the ferromagnetic Mn^{4+}-O-Mn^{3+} superexchange path and that the rest of Mn ions contribute to paramagnetism with antiferromagnetic coupling. Since the antiferromagnetic superexchange interaction of the Mn^{3+}-O-Mn^{3+} path is predominant in the area of sparse hole carriers, the Weiss temperature becomes negative. In the insulating LSMO heterostructure, the thickness of the magnetic dead layer is determined by the strain-relaxed region near the heterointerface because magnetic anisotropy due to the superexchange interaction strongly depends on strain.

Finally, experimental findings that the changes in magnetic behavior concomitant with the MIT may suggest applications of ferromagnetic oxide interfaces. In contrast to the magnetic dead layer of about 4 u.c. in the LSMO/STO interfaces reported previously [17,18], the present heterostructure with a thin LSMO layer of 5 u.c. shows ferromagnetism, maybe due to the significantly improved crystal quality and sandwiching LSMO between LAO and STO layers. The appearance of ferromagnetism in such precisely controlled heterostructures at the atomic level will contribute to the development of nanometer-scale spintronic device applications. If one can control the position of E_F in the LSMO layer by applying a bias voltage, the magnetic behavior will change, depending on the hole concentration in the LSMO layer. This may be analogous to the orbital-controlled magnetization switching observed in a LSMO/STO/LSMO magnetic tunnel junction [10]. Additionally, based on the present SQUID, STEM, and XMCD results, the magnetic behavior observed for $t = 5$ u.c. reflects the LSMO layer under compressive strain. It should be noted here that the top LAO layer significantly affects the magnetic behavior in the insulating LSMO layer, even though the thickness of the LAO layer is merely 2 u.c. thick. This indicates that the structural design of ferromagnetic oxide heterostructures on the nanometer scale possibly controls the performance or properties of such devices.

IV. CONCLUSIONS

The magnetic anisotropy strongly changes with the LSMO thickness due to the delicate balance between strains originating from both the Nb:STO and LAO layers in epitaxially grown single-crystalline $LaAlO_3$(2 u.c.)/$La_{0.6}Sr_{0.4}MnO_3$(t u.c.)/Nb:$SrTiO_3$(001) heterostructures with varying LSMO layer thickness, t. The film with $t = 5$ u.c. has perpendicular magnetic anisotropy, while that with $t = 15$ u.c. has in-plane magnetic anisotropy. Structural analysis using STEM EELS has revealed that the 5-u.c. LSMO layer is compressively strained, while the 15-u.c. LSMO layer is under tensile strain. To understand the interfacial magnetic and electronic properties of the LAO/LSMO/Nb:STO heterostructures with different LSMO thicknesses, we perform XMCD and PES measurements. The observation of the well-screened features in the Mn $2p$ XPS spectra suggests a significantly improved crystal-structure quality at the interface between the LAO and LSMO layers in the MBE-grown thin films. The Mn $L_{2,3}$ XMCD and Mn $2p$-$3d$ RPES demonstrate the change of the magnetic behavior accompanied by the MIT. The magnetic behavior of the insulating thin LSMO layer originates from the superexchange interaction between the Mn ions under compressive strain from the top LAO layer, while the double-exchange interaction is predominant in the ferromagnetic metallic LSMO layer. Based on the present experimental findings, the formation of the magnetic dead layer is attributed to competition between the superexchange and double-exchange interactions in the strain-relaxed region near the heterointerface. It is likely that the appearance of the ferromagnetic properties in the heterostructure with such thin LSMO layers and the changes in the magnetic behavior concomitant with the MIT provide key aspects of ferromagnetic oxide heterostructures for structural design on the nanometer scale and spintronic device applications.

ACKNOWLEDGMENTS

This work is supported by Grants-in-Aid for Scientific Research (Grants No. 18H03860 and No. 19K21960) from the Japan Society for the Promotion of Science (JSPS) and PRESTO Program (Grants No. JPMJPR19LB and No. JPMJCR1777) of Japan Science and Technology Agency (JST), Japan. This work is partially supported the Spintronics Research Network of Japan (Spin-RNJ). This work is performed under the Shared Use Program of the Japan Atomic Energy Agency (JAEA) Facilities (Proposals No. 2017B-E19 and No. 2020A-E18) supported by the JAEA Advanced Characterization Nanotechnology Platform as a program of the "Nanotechnology Platform" of the Ministry of Education, Culture, Sports, Science and Technology (MEXT) (Proposals No. A-17-AE-0038 and No. JPMXP09A20AE0018). The experiment at SPring-8 is approved by the Japan Synchrotron Radiation Research Institute (JASRI) Proposal Review Committee (Proposals No. 2017B3841 and No. 2020A3841).

[1] H. Y. Hwang, Y. Iwasa, M. Kawasaki, B. Keimer, N. Nagaosa, and Y. Tokura, Emergent phenomena at oxide interfaces, Nat. Mater. **11**, 103 (2012).

[2] A. Ohtomo, D. A. Muller, J. L. Grazul, and H. Y. Hwang, Artificial charge-modulation in atomic-scale perovskite titanate superlattices, Nature **419**, 378 (2002).

[3] H. Takagi and H. Y. Hwang, An emergent change of phase for electronics, Science **327**, 1601 (2010).

[4] J. Mannhart and D. G. Schlom, Oxide interfaces–an opportunity for electronics, Science **327**, 1607 (2010).

[5] L. D. Anh, S. Kaneta, M. Tokunaga, M. Seki, H. Tabata, M. Tanaka, and S. Ohya, High-mobility 2D hole gas at a $SrTiO_3$ interface, Adv. Mater. **32**, 1906003 (2020).

[6] M. Bowen, M. Bibes, A. Barthélémy, J.-P. Contour, A. Anane, Y. Lemaître, and A. Fert, Nearly total spin polarization in $La_{2/3}Sr_{1/3}MnO_3$ from tunneling experiments, Appl. Phys. Lett. **82**, 233 (2003).

[7] S. M. Wu, S. A. Cybart, P. Yu, M. D. Rossell, J. X. Zhang, R. Ramesh, and R. C. Dynes, Reversible electric control of exchange bias in a multiferroic field-effect device, Nat. Mater. **9**, 756 (2010).

[8] R. Werner, A. Yu. Petrov, L. Alvarez Miño, R. Kleiner, D. Koelle, and B. A. Davidson, Improved tunneling magnetoresistance at low temperature in manganite junctions grown by molecular beam epitaxy, Appl. Phys. Lett. **98**, 162505 (2011).

[9] L. D. Anh, N. Okamoto, M. Seki, H. Tabata, M. Tanaka, and S. Ohya, Hidden peculiar magnetic anisotropy at the interface in a ferromagnetic perovskite-oxide heterostructure, Sci. Rep. **7**, 8715 (2017).

[10] L. D. Anh, T. Yamashita, H. Yamasaki, D. Araki, M. Seki, H. Tabata, M. Tanaka, and S. Ohya, Ultralow-Power Orbital-Controlled Magnetization Switching Using a Ferromagnetic Oxide Interface, Phys. Rev. Appl. **12**, 041001(R) (2019).

[11] L. Fitting Kourkoutis, J. H. Song, H. Y. Hwang, and D. A. Muller, Microscopic origins for stabilizing room-temperature ferromagnetism in ultrathin manganite layers, Proc. Natl. Acad. Sci. **107**, 11682 (2010).

[12] A. Urushibara, Y. Moritomo, T. Arima, A. Asamitsu, G. Kido, and Y. Tokura, Insulator-metal transition and giant magnetoresistance in $La_{1-x}Sr_xMnO_3$, Phys. Rev. B **51**, 14103 (1995).

[13] J.-H. Park, E. Vescovo, H.-J. Kim, C. Kwon, R. Ramesh, and T. Venkatesan, Direct evidence for a half-metallic ferromagnet, Nature **392**, 794 (1998).

[14] M. Imada, A. Fujimori, and Y. Tokura, Metal-insulator transitions, Rev. Mod. Phys. **70**, 1039 (1998).

[15] Y. Tokura and Y. Tomioka, Colossal magnetoresistive manganites, J. Magn. Magn. Mater. **200**, 1 (1999).

[16] Y. Konishi, Z. Fang, M. Izumi, T. Manako, M. Kasai, H. Kuwahara, M. Kawasaki, K. Terakura, and Y. Tokura, Orbital-state-mediated phase-control of manganites, J. Phys. Soc. Jpn. **68**, 3790 (1999).

[17] K. Yoshimatsu, K. Horiba, H. Kumigashira, E. Ikenaga, and M. Oshima, Thickness dependent electronic structure of $La_{0.6}Sr_{0.4}MnO_3$ layer in $SrTiO_3/La_{0.6}Sr_{0.4}MnO_3/SrTiO_3$ heterostructures studied by hard x-ray photoemission spectroscopy, Appl. Phys. Lett. **94**, 071901 (2009).

[18] M. Izumi, Y. Ogimoto, T. Manako, M. Kawasaki, and Y. Tokura, Interface effect and Its doping dependence in $La_{1-x}Sr_xMnO_3/SrTiO_3$ superlattices, J. Phys. Soc. Jpn. **71**, 2621 (2002).

[19] Y. H. Sun, Y. G. Zhao, H. F. Tian, C. M. Xiong, B. T. Xie, M. H. Zhu, S. Park, W. Wu, J. Q. Li, and Q. Li, Electric and magnetic modulation of fully strained dead layers in $La_{0.67}Sr_{0.33}MnO_3$ films, Phys. Rev. B **78**, 024412 (2008).

[20] Y. Zhu, K. Du, J. Niu, L. Lin, W. Wei, H. Liu, H. Lin, K. Zhang, T. Yang, Y. Kou, J. Shao, X. Gao, X. Xu, X. Wu, S. Dong, L. Yin, and J. Shen, Chemical ordering suppresses large-scale electronic phase separation in doped manganites, Nat. Commun. **7**, 11260 (2016).

[21] G. Shibata, K. Yoshimatsu, E. Sakai, K. Ishigami, S. Sakamoto, Y. Nonaka, F.-H. Chang, H.-J. Lin, D.-J. Huang, C.-T. Chen, H. Kumigashira, and A. Fujimori, Temperature evolution of magnetic phases near the thickness-dependent metal–insulator transition in $La_{1-x}Sr_xMnO_3$ thin films observed by XMCD, JPS Conf. Proc. 30, 011072 (2020).

[22] A. Yokoya, T. Sekiguchi, Y. Saitoh, T. Okane, T. Nakatani, T. Shimada, H. Kobayashi, M. Takao, Y. Teraoka, Y. Hayashi, S. Sasaki, Y. Miyahara, T. Harami, and T. A. Sasaki, Soft X-ray beamline specialized for actinides and radioactive materials equipped with a variably polarizing undulator, J. Synchrotron Radiat. **5**, 10 (1998).

[23] J. Okamoto, K. Mamiya, S.-I. Fujimori, T. Okane, Y. Saitoh, Y. Muramatsu, A. Fujimori, S. Ishiwata, and M. Takano, Magnetic circular X-ray dichroism study of paramagnetic and anti-ferromagnetic states in $SrFeO_3$ using a 10-T superconducting magnet, AIP Conf. Proc. **705**, 1110 (2004).

[24] Y. Saitoh, Y. Fukuda, Y. Takeda, H. Yamagami, S. Takahashi, Y. Asano, T. Hara, K. Shirasawa, M. Takeuchi, T. Tanaka, and H. Kitamura, Performance upgrade in the JAEA actinide science beamline BL23SU at SPring-8 with a new twin-helical undulator, J. Synchrotron Radiat. **19**, 388 (2012).

[25] A. Tanaka and T. Jo, Resonant 3d, 3p and 3s photoemission in transition metal oxides predicted at 2p threshold, J. Phys. Soc. Jpn. **63**, 2788 (1994).

[26] C. Aruta, G. Ghiringhelli, V. Bisogni, L. Braicovich, N. B. Brookes, A. Tebano, and G. Balestrino, Orbital occupation, atomic moments, and magnetic ordering at interfaces of manganite thin films, Phys. Rev. B **80**, 014431 (2009).

[27] W. A. Harrison, *Electronic Structure and Physical Properties of Solids* (Freeman, San Francisco, 1980).

[28] G. Shibata, et al., Anisotropic spin-density distribution and magnetic anisotropy of strained $La_{1-x}Sr_xMnO_3$ thin films: Angle-dependent x-ray magnetic circular dichroism, npj Quantum Mater. **3**, 3 (2018).

[29] K. Horiba, et al., Nature of the Well Screened State in Hard X-Ray Mn 2*p* Core-Level Photoemission Measurements of $La_{1-x}S_xMnO_3$ Films, Phys. Rev. Lett. **93**, 236401 (2004).

[30] T. Pincelli, et al., Quantifying the critical thickness of electron hybridization in spintronics materials, Nat. Commun. **8**, 16051 (2017).

[31] G. Shibata, K. Yoshimatsu, E. Sakai, V. R. Singh, V. K. Verma, K. Ishigami, T. Harano, T. Kadono, Y. Takeda, T. Okane, Y. Saitoh, H. Yamagami, A. Sawa, H. Kumigashira, M. Oshima, T. Koide, and A. Fujimori, Thickness-dependent ferromagnetic metal to paramagnetic insulator transition in $La_{0.6}Sr_{0.4}MnO_3$ thin films studied by x-ray magnetic circular dichroism, Phys. Rev. B **89**, 235123 (2014).

[32] S. Valencia, L. Paña, Z. Konstantinovic, L. Balcells, R. Galceran, D. Schmitz, F. Sandiumenge, M. Casanove, and B. Martínez, Intrinsic antiferromagnetic/insulating phase at manganite surfaces and interfaces, J. Phys.: Condens. Matter **26**, 166001 (2014).

[33] B. Cui, S. Song, F. Li, G. Y. Wang, H. J. Mao, J. J. Peng, F. Zeng, and F. Pan, Tuning the entanglement between orbital reconstruction and charge transfer at a film surface, Sci. Rep. **4**, 4206 (2014).

[34] F. Tsui, M. C. Smoak, T. K. Nath, and C. B. Eom, Strain-dependent magnetic phase diagram of epitaxial $La_{0.67}Sr_{0.33}MnO_3$ thin films, Appl. Phys. Lett. **76**, 2421 (2000).

[35] C. Zener, Interaction between the *d*-shells in the transition metals. II. Ferromagnetic compounds of manganese with perovskite structure, Phys. Rev. **82**, 403 (1951).

[36] J. B. Goodenough, A. Wold, R. J. Arnott, and N. Menyuk, Relationship between crystal symmetry and magnetic properties of ionic compounds containing Mn^{3+}, Phys. Rev. **124**, 373 (1961).

[37] T. K. Nath, R. A. Rao, D. Lavric, and C. B. Eom, Effect of three-dimensional strain states on magnetic anisotropy of $La_{0.8}Ca_{0.2}MnO_3$ epitaxial thin films, Appl. Phys. Lett. **74**, 1615 (1999).

[38] Y. Feng, K.-J. Jin, L. Gu, X. He, C. Ge, Q.-H. Zhang, M. He, Q.-L. Guo, Q. Wan, M. He, H.-B. Lu, and G. Yang, Insulating phase at low temperature in ultrathin $La_{0.8}Sr_{0.2}MnO_3$ films, Sci. Rep. **6**, 22382 (2016).

[39] C. L. Jia, S. B. Mi, M. Faley, U. Poppe, J. Schubert, and K. Urban, Oxygen octahedron reconstruction in the $SrTiO_3/LaAlO_3$ heterointerfaces investigated using aberration-corrected ultrahigh-resolution transmission electron microscopy, Phys. Rev. B **79**, 081405(R) (2009).

[40] T. T. Fister, H. Zhou, Z. Luo, S. S. A. Seo, S. O. Hruszkewycz, D. L. Proffit, J. A. Eastman, P. H. Fuoss, P. M. Baldo, H. N. Lee, and D. D. Fong, Octahedral rotations in strained $LaAlO_3/SrTiO_3$ (001) heterostructures, APL Mater. **2**, 021102 (2014).